Article

A Novel Cooling Design for an Agonistic–Antagonistic SMA Tendon-Driven Actuator

Renke Liu [1], Shuyao Zhang [1], Yusuke Baba [1] and Hideyuki Sawada [2,*]

[1] Department of Pure and Applied Physics, Waseda University, Tokyo 169-8555, Japan;
     askar_liu@fuji.waseda.jp (R.L.)
[2] Faculty of Science and Engineering, Waseda University, Tokyo 169-8555, Japan
*   Correspondence: sawada@waseda.jp

Abstract: Shape memory alloys (SMAs) exhibit a unique property that undergoes deformation in response to temperature variation. This characteristic can be utilized via the application of a filiform SMA wire to tendon-driven robotic actuators for biomimetic joint movements. However, due to the inefficiencies in heat dissipation, conventional SMA tendon-driven actuators are characterized by their lower relaxation speeds than other actuators. This paper proposes a novel cooling design for an SMA tendon-driven actuator using thin-fin heat sinks based on a multi-layer wrapped SMA tendon design. In addition, the electric circuit and the controller are refined. Prototype devices are constructed to validate the performance of SMA-based actuators under PID control. The results indicate that the proposed design exceeds previous models in terms of relaxation performance by up to 5.8 times while also being able to stabilize at a target angle within 0.5 s under control.

Keywords: biomimetic robotics; tendon actuator; shape memory alloys

1. Introduction

Shape memory alloys (SMAs) were first discovered in the 1970s by Arne Ölander [1]. They are distinctive alloys that retain memories of their original shape. Composed of various metals, SMAs possess unique characteristics of the shape memory effect and display pseudo-elastic phenomena. When subjected to the shape memory effect, SMA material transitions from the Martensite phase to the Austenite phase as the crystal temperature surpasses the transformation point. According to Kikuaki Tanaka et al. [2], an SMA can be deformed via an external force in the Martensite phase at a lower temperature and returns to a remembered shape in the Austenite phase at a higher temperature when heated beyond the transforming point. The pseudo-elasticity phenomena, also known as superelasticity, usually occur in the Austenite phase, enabling SMA material to potentially return to its standard shape after the removal of mechanical stress or strain.

Under the influence of the shape memory effect and pseudo-elastic phenomena, SMA material becomes a good foundation for introducing novel actuators and driving robots, especially in systems requiring small sizes. Due to these characteristics, SMA has been widely applied as an actuator in various fields, such as robotics [3,4], medical devices [5], and aerospace fields [6,7]. Compared to other devices driven by traditional methods, it shows a superior high power-to-weight ratio and density.

O. Benafan et al. introduced the application of rotary shape memory alloy actuators in the field of aviation, while the spanwise adaptive wing (SAW) project and the wind tunnel remote control actuation (RCA) are new applications that utilize recent advancements [8]. Peter L. Bishay et al. introduced MataMorph-3, a fully deformable unmanned aerial vehicle (UAV) with wing curvature and tail stabilizers [9]. The skin sliding concept provides a reliable solution for stretchable skin in morphing aircraft design.

SMA materials also play a crucial role in prosthetic arm design. The year 2021 saw the introduction of a novel system known as the 'Clever Lever & Locking' (CLL) system [10].

The system amplifies the stroke of SMA wire actuators in a prosthetic forearm and locks them post-actuation to conserve energy. Konstantinos Andrianesis et al. introduced a low-cost prosthetic hand, using shape memory alloys to achieve compact and silent actuation. This device featured improved size, weight, and noise levels, enhancing usability for upper-limb amputees [11]. Enrique Soriano-Heras et al. developed a novel concept centered around modular prosthetic hands with rapid prototyping and new SMA actuators, minimizing manufacturing costs [12]. MataPro-1 was designed by Peter L. Bishay et al. in 2020 [13]. This device featured a 3D-printed hand with flexible joints, shape memory alloy (SMA) wires for grip strength, and realistic silicone flesh. SMA wires were cooled in the forearm, enabling noise-free operation. Vishalini Bundhoo [14] and Gabriele Gilardi [15] presented an SMA-wire-driven biomimetic robot finger. The performance was tested using a 4-DoF test bench and the results showed that the researchers successfully imitated the joint movements and trajectory of a human finger, with SMA wires taking 20 to 30 s to cool down from the activated state.

The phase transformation of SMA wires occurs when temperature changes, whereas most devices suffer from slow cooling, which limits their responsiveness. The discussion around enhancing the performance of SMA-driven robotics has centered on developing cooling systems. Shing Shin Cheng [16] demonstrated a method employing water flow where a silicone tube is placed in an SMA spring and filled with liquid, resulting in a significantly improved cooling performance. However, the system became more complicated and heavier due to the inclusion of a water pump, a water reservoir, and a special seal to prevent water leakage. Therefore, developing a cooling system that enables high activation frequency with a simple structure is essential to using SMA actuators in robotics.

Seong Jun Park [17] introduced a fabric muscle exosuit woven from SMA springs and wires. Benefiting from the woven structure and the high power density of SMA material, the proposed device could reduce muscle activity by approximately 50–70% when holding a 10 kg weight. By introducing forced-air convection fans into the woven actuator, he successfully improved the relaxation performance and achieved a 90% reduction in relaxation time to 5.6 s [18].

Renke Liu [19] demonstrated an antagonistic SMA wire-driven robotic finger with a simple design and lightweight. By wrapping multiple layers of material outside the SMA wire, they successfully provided electrical insulation for the SMA wire without significantly slowing activation speed. However, the performance of the SMA actuator was not formally discussed in comparison to former designs. Furthermore, the performance of their proposed actuators remains unsatisfactory.

This study explores the thermal performance of SMA-driven tendon actuators in order to enhance their responsiveness for possible biomimetic applications. We propose a novel cooling design based on a multi-layer wrapped SMA wire strategy. This functions by employing small-form-factor copper fin heat sinks and providing force convection with centrifugal fans. Based on the proposed idea, we build validation robotic joint prototypes, and experiments are performed with controlled conditions. A high-refresh-rate, multi-processed testing system, refined from previously established real-time feedback sensing and control systems, is developed to assess the proposed cooling concept rigorously. The proposed cooling concept is validated by testing the prototype devices, driven by a refined electric system. The result indicates an improvement in the responsiveness of the former SMA tendon actuator, with the new device providing a feedback-controlled activation that stabilizes within 0.5 s, while balancing weight, fast acceleration, and high relaxation speed.

2. Design Concepts of SMA Actuator

2.1. SMA-Tendon-Driven Actuator

Compared with traditional materials, SMA materials change shape following changes in body temperature. Utilizing this characteristic, pre-shaped SMA material can be used to make movements. Usually, the alloy possesses a relatively lower temperature at the initial stage, where the SMA and connected mechanical systems stay static. When actuation is

required, heat is applied to the SMA material, typically via powering the alloy with electric current, either directly or indirectly. With the increasing material temperature, the metal state shifts to the Austenite site and causes a change in shape, which drives the mechanical part. This process is also known as electrical Joule heating actuation.

When activation is finished, it is usually necessary to retain the same activated state for a certain period. At this sustaining stage, powering SMA with a lower but sustained electric current is often considered due to heat conduction. To complete a full working cycle, the device must be powered off. This results in a cooling down and slow return of the metal state to the Martensite state. Under a sufficient bias force, the mechanical system can return to its initial state, completing the actuating–sustaining–relaxing cycle. The SMA material has been previously applied to robotic joints as a driving tendon for rotational motions. Unlike conventional actuating methods such as motors, cylinders, and piezoelectric actuators, heating–sustaining–cooling-controlled motion and inherent deflection–relaxation behaviors of SMA materials can induce biomimetic motion, offering a possible approach to achieving controlled biomimetic mechanisms.

In the preceding study [19], a simple structure of an SMA-tendon-driven actuator was introduced, as depicted in Figure 1. Combined with two connected sides, the motion side and the fixed side, the actuator was able to provide movement under the fast contraction speed of the SMA wire. The motion-side beam is mounted onto a spindle and can rotate around the joint, providing directly driven motion. During actuation, the fixed side is held by a bracket in order to provide a continuous opposing force. Connected to the SMA wire, the adjusting gear at one end exists in order to adjust the initial wire length for the purpose of compensating for manufacturing variances. During actuation, a controlled electric current is applied to the SMA wire. This generates Joule heat, increasing the wire temperature and length contraction. This contraction allows the SMA wire to function as a tendon and muscle, forcing the motion side to lean toward the fixed side, creating a rotational motion and lifting the load hanging at the tip. With the large effort to load arm ratio, the small deflection motion of the SMA tendon can be enlarged to a wide range of motion.
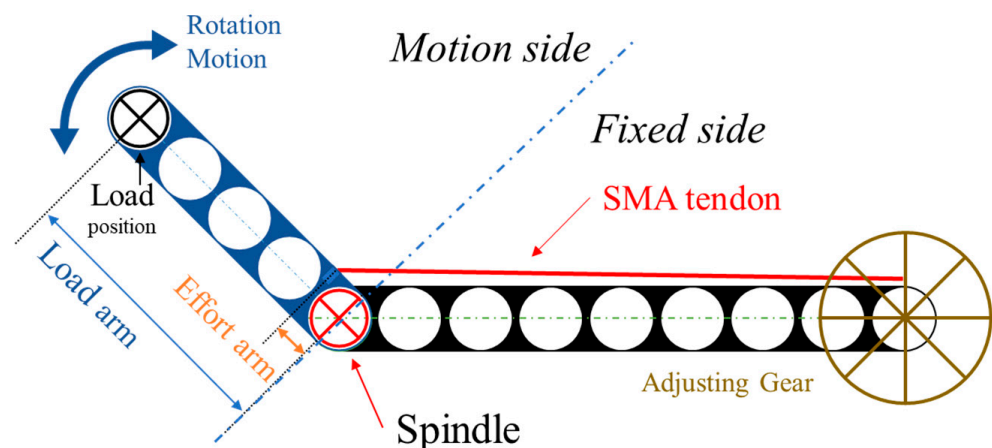

Figure 1. Illustration of SMA-tendon-driven actuator.

Figure 2 illustrates an agonistic–antagonistic design of an SMA-driven actuator, where an SMA tendon is added to both sides of the robotic joint. The upper SMA tendon works as a flexor muscle, dragging the motion side toward the fixed side, while the lower extensor SMA pulls the motion side away from the fixed. Through such process, the deflection angle can be controlled. Each SMA tendon is connected to a single adjusting gear in order to alter the initial length.
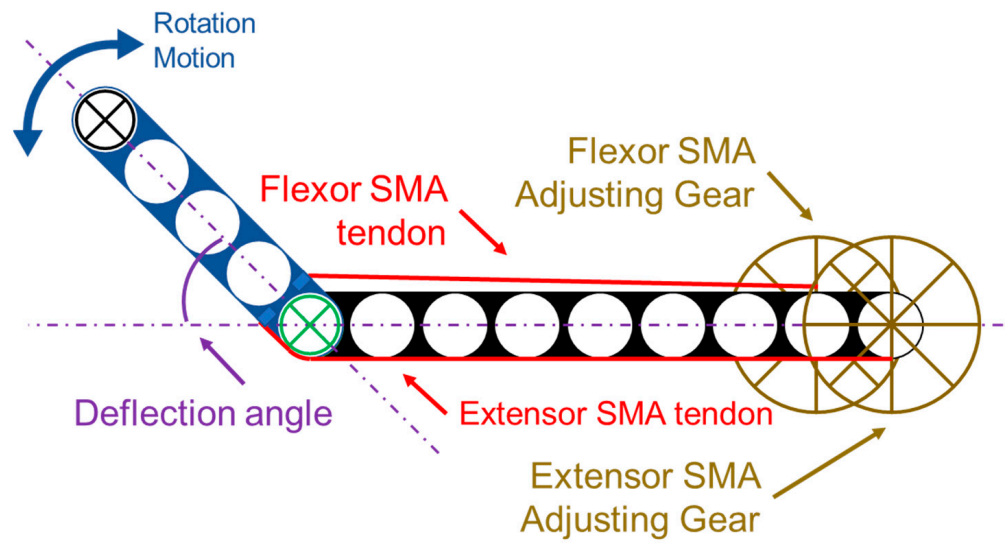
Figure 2. The antagonistic design of SMA-tendon-driven actuator.

With agonistic–antagonistic pairs, a robotic joint can move in two directions with one degree of freedom. The current deflection angle θ_t is defined as the delta angle of the motion side being dragged towards the fixed side along the flexor direction. At the initial state, the deflection angle is $\theta_0 = 0°$. Considering tendon length for current joint deflection angle θ_t, a mathematical model can be built to predict the required length of SMA wire $l(\theta_t)$.

Figure 3 illustrates a mathematical model of the SMA-tendon-driven actuator joint. When an SMA wire is used as a flexor, as shown in Figure 3a, the required wire length l_{SMA} can be calculated as:

$$l_{SMA} = \sqrt{l_L{}^2 + l_F{}^2 + 2r^2 - 2(l_L + l_F)r\sin\theta_t + (2l_Ll_F - 2r^2)\cos\theta_t} \tag{1}$$

where $\theta_t \in [0, \pi)$ stands for current deflection angle. l_L and l_F demonstrate the length to the center where the SMA tendon is locked on for the lever and fixed sides. Detailed proof is shown in Appendix A.
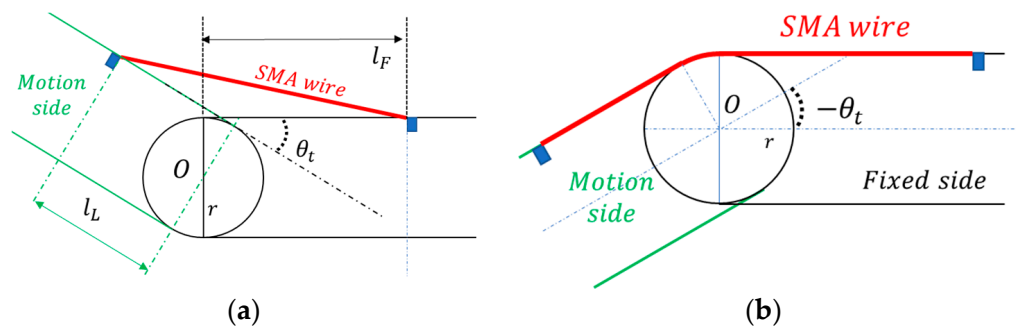

Figure 3. Mathematical modeling of tendon actuator: (**a**) SMA wire configured as flexor tendon; (**b**) SMA wire configured as extensor tendon.

As shown in Figure 3b, when used as an extensor tendon, an SMA wire is blocked by the round end of the beam, rendering the required wire length as:

$$l_{SMA} = l_L + l_F - \theta_t r \tag{2}$$

where $\theta_t \in (-\pi, 0)$.

2.2. Improved Cooling Concept

The SMA-driven mechanism can be activated once again after it finishes the full relaxation stage. Otherwise, the range of motion will be reduced since the metal has not fully returned to its initial shape. Thus, the improvement in relaxation speed has significant meaning. Wire-shaped SMA alloys have been applied in many fields on account of their higher surface-volume ratios than those of thin plate-shaped variants of identical thickness. When considering passive cooling methods for application in tendon-driven actuators, a larger surface of SMA wire can lead to a higher cooling rate, leading to a shortened delay or a larger range of motion for the next actuation cycle.

When seeking to improve the cooling design of an SMA tendon actuator for robots, one of the common difficulties faced is the conductivity of the SMA wire's surface. Unlike copper coils, SMA wire works in a regular- and shrunk-state circulation. If a typical silicon coating is added for insulation, silicon wrapping is constantly compressed due to stickiness between contacting surfaces. The passive shrinkage of silicon causes a waste of energy, and waste heat generated in such a process further hinders the cooling effect. A multi-layered wrapping design from [19] is utilized to address this issue, as shown in Figure 4a.
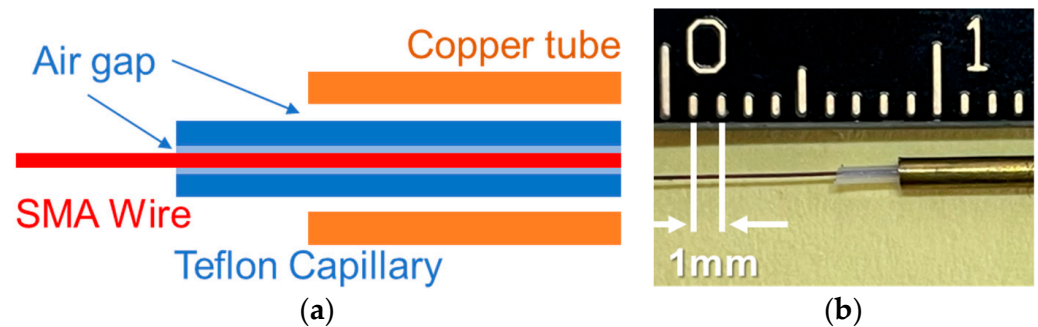

Figure 4. The multi-layered wrapping of SMA wire: (**a**) Illustration of multi-layered wrapping; (**b**) the wrapped SMA wire.

Figure 4 shows a wrapped SMA wire for the actuator, with an SMA wire of 0.15 mm diameter. Table 1 shows the inner and outer diameters of the Teflon capillary and copper tube. The copper tube wrapping outside the Teflon helps to conduct heat for better heat dissipation while also providing solid protection for the soft SMA wire and Teflon capillary. The inner diameter of the Teflon capillary and copper tube are selected so that the SMA wire can be smoothly inserted into the Teflon capillary while maintaining a small tube thickness. The small air gap between the SMA wire and the Teflon capillary lower the friction during actuation process.

Table 1. The physical size of Wrapping tubes.

Parts	Diameter	Value
SMA wire	Inner	-
	Outer	0.15 mm
Teflon Capillary	Inner	0.2 mm
	Outer	0.6 mm
Copper Tube	Inner	0.7 mm
	Outer	1.2 mm

The formula $Q/t = hA\Delta T$ can be used to consider the heat transfer rate between the SMA wire-based actuator and room temperature air. h is the heat transfer coefficient, A is the contact surface area, and ΔT is the temperature difference between exposed SMA wire and air. Considering that the relaxation process of SMA wire is positively related to heat transferring rate Q/t, increasing the heat transferring coefficient, surface area, and

temperature variation can help to improve the actuator's performance during the relaxation process.

If considering increasing temperature difference $\Delta T = T_{SMA} - T_{air}$, it is noticed that SMA phase changing is directly related to the material temperature, which affects the surface temperature T_{SMA}. Increasing T_{SMA} may disrupt SMA wires' phase-changing state in each working cycle, decreasing relaxing performance. On the other hand, if T_{air} decreases, external supporting parts such as pump-based coolers, thermoelectric (TEC) coolers, or vortex tubes are required. Each of these not only possesses significant weight but also necessitates substantial energy consumption. Thus, this study considers increasing the air-contacting surface while less substantially increasing size and weight.

The contacting surface of an exposed SMA wire can be considered $A_{SMA} = \pi d_{SMA} l_{SMA}$, where $d_{SMA} = 0.15$ mm is the outer diameter of the used SMA wire, and l_{SMA} is the length. For a 1 mm long SMA wire, the contacting surface area is $A_{SMA} \approx 0.471$ mm^2. For multi-layer wrapped SMA wire, the contacting surface area is $A_{CTSMA} \approx 3.770$ mm^2.

To induce a further increase in air-contacting area, a heat sink made of copper fins is incorporated into the actuator, as shown in Figure 5. The illustrated copper fin possesses a characteristic width of 13.0 mm and height of 7.60 mm; the implement is constructed from 0.20 mm thick copper fins via punch molding. A 10 cm long heat sink comprises 68 individual cooling fins. Through calculation, the contacting surface area is approximately 175.57 mm^2 per millimeter in length, which is around 45 times larger than a multi-layer solution. The weight of the heat sink is 1.06 g per millimeter. Figure 5b illustrates a soldered, multi-layer wrapped structure, with enhanced thermal conductivity between the copper tube and heat fins.
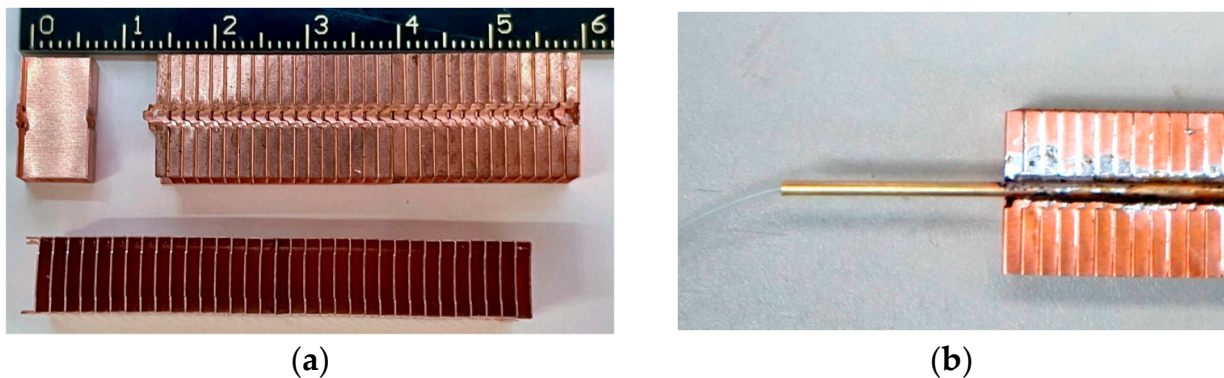

(a)   **(b)**

Figure 5. The copper fin for increasing contacting surface: (**a**) The copper fin; (**b**) multi-layer wrapped SMA soldered on a copper heat sink.

Enhancing the velocity of airflow is another strategy for increasing heat dissipation. As shown in Figure 6, DC fans are utilized to induce forced convection, thereby elevating airflow. The incorporated centrifugal fan is powered by a DC motor, providing up to 8000 rpm rotation, generating airflow for around 1.5 cubic feet per minute (CFM), and producing approximately 8.52 mmAq of static pressure. Compared with an axial fan, a centrifugal fan has the advantage of generating higher pressure, compensating for the increased air resistance generated by extensive heat fins.
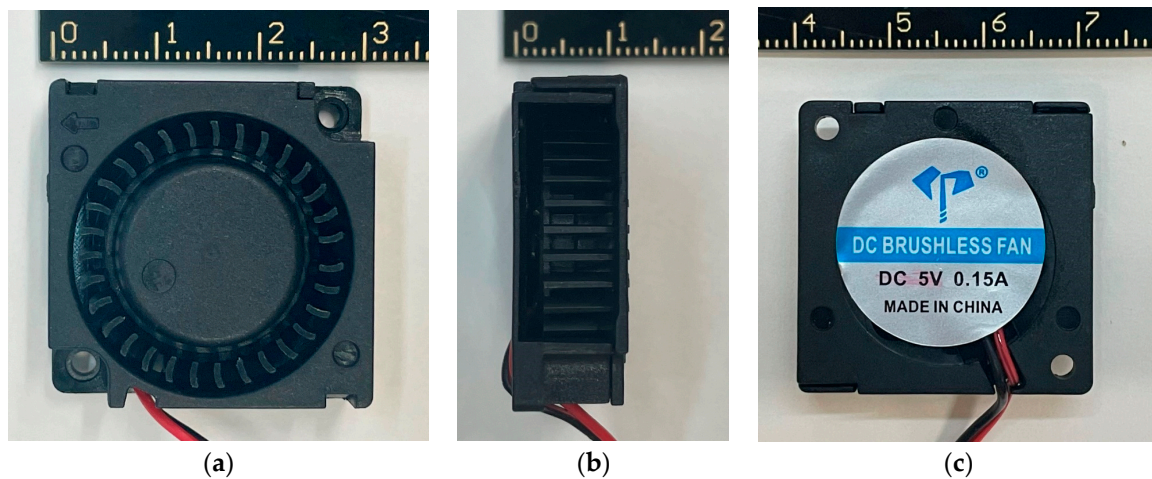
Figure 6. The incorporated DC brushless centrifugal fan for forced convection: (**a**) Top view; (**b**) side view of ventilation port; (**c**) bottom view.

3. SMA-Based Tendon-Driven Actuator

3.1. Single Joint Actuator

The SMA wire used in this study is Biofiber BMF-150 from Toki Corporation. As shown in Table 2, the BMF-150 wire has a typical diameter of 0.15 mm and can sustain 1.8 kg of tension. A destructive tensile test shows that a single BMF-150 wire can survive tension of over 2 kg in the longitudinal direction.

Table 2. Specification of Biofiber BMF-150 SMA wire.

Feature	Value	Unit
Diameter	0.15	mm
Weight	112	mg/m
Standard Resistance	61	Ω/m
Standard Driving Voltage	20.7	V/m
Standard Driving Current	0.34	A
Standard Power Consumption	7.05	W/m
Practical Strain	4.0	%
Practical Life Cycles (Under 80 Mpa)	$> 10^6$	times
Destruction Force	1.8	kgf

To simplify the manufacturing process, facilitate structural adjustments, and prepare experiments, the construction of the actuator primarily utilizes Lego Technic bricks. A modified 7-hole Lego beam is used on the motion side, as shown in Figure 7. Compared with the original Lego brick presented in Figure 7b, the modified version incorporates one additional cross-hole at the end of the beam, following Lego cross-hole dimensions. A cross-mount adapter is designed to accommodate the installation of a cross shaft connecting the rotary encoder.

Figure 8 illustrates a 3D-modeled and 3D-printed cross shaft connecting the rotational center of the motion side beam and a rotary encoder. The T-shaped terminus of the shaft can fit inside a mounting hole of the rotary encoder without wobbling in the rotating direction. Both the beam and cross shaft are 3D-printed with PLA by a Creality-K1 printer, with a layer height of 0.2 mm and nozzle diameter of 0.4 mm.
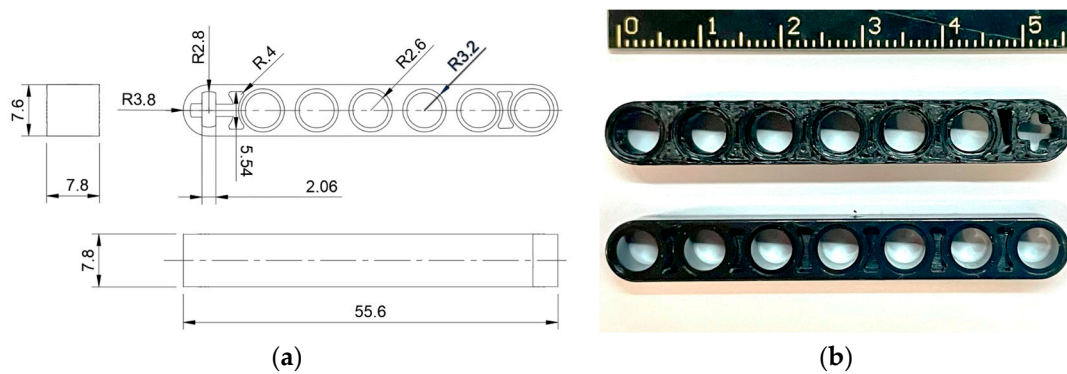
Figure 7. The 3D-printed motion side beam: (**a**) Dimensional diagram of a 3D-printed beam (mm); (**b**) 3D-printed motion arm (**upper**) and original Lego beam (**lower**).
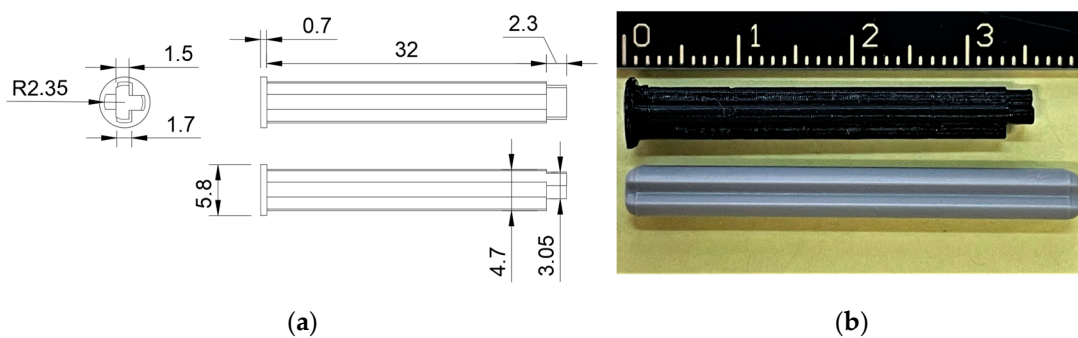

Figure 8. The eccentric shaft for installation of rotary encoder: (**a**) The orthographic projections; (**b**) the 3D-printed shaft compared with the original Lego shaft.

Figure 9 shows a single-wired actuator cooled by the proposed design hold horizontally on a test stand. A 360 dial is used only for calibrating a rotary sensor, which will be introduced latter. A 50 mm long and 0.05 mm thick copper tape is applied to the end of the beam to protect the Lego ABS plastic from melting. A set of copper rivets is utilized to secure the SMA wire to the end of the motion side, and an original Lego cross shaft coupled with a Lego cross sleeve is used to secure the SMA wire onto the fixed side, analogous to the method introduced in [19]. Destructive tests show that the securing method can avoid relative sliding over 2 Kgf.

The length of the SMA wire is 112.0 mm. The copper tube wrapping the SMA wire is 100 mm long, the same length as the heat sink. The inner Teflon capillary is 102 mm, extending 1 mm beyond copper on both ends to protect the SMA wire from short-circuiting.

3.2. Prototype for Agonistic–Antagonistic Actuation

To assess the responsiveness of the actuator with the proposed cooling design, an agonistic–antagonistic SMA actuator containing two opposing SMA wires is constructed, as illustrated in Figure 10.

The antagonist actuator contains an SMA tendon on both sides, enabling active motion control. On the flexor side, the length of the SMA wire, the multi-layer wrapping, and the adjusting mechanism are identical to those specified for the design in Section 3.1. On the extensor side, the SMA wire is 7.8 mm shorter in order to prevent contact between the flexor and extensor adjusting gears, as shown in Figure 10a.

Both extensor side and flexor side SMA wire are cooled by a 100 mm long heatsink ventilated by a centrifugal fan guided by an air deflector, as shown in Figure 10b. Insulating tapes are used for preventing air leakage. Figure 11 illustrates the detailed design of the air deflector which features an expanding exhaust, positioned facing the heat sink fins to direct the airflow.
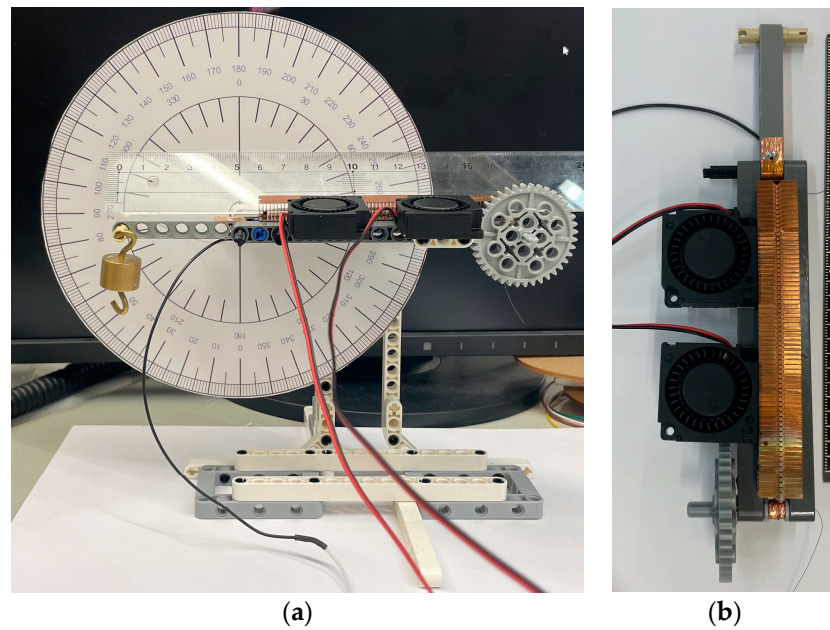
Figure 9. The testing single joint SMA-tendon driven actuator placed on a testing racket built by Lego Technic bricks: (**a**) The actuator placed on a testing racket with a dial; (**b**) an upper view of the actuator.
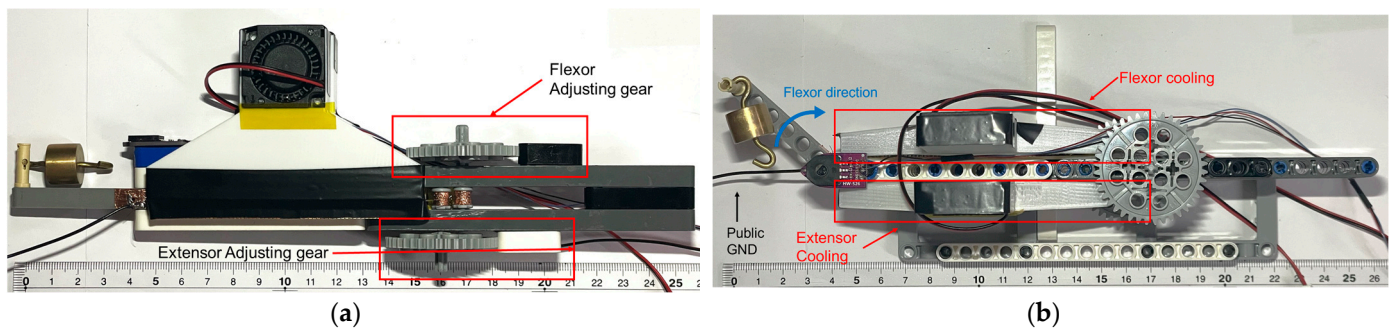

Figure 10. The prototype agonistic–antagonistic joint: (**a**) Upper view of test actuator; (**b**) the antagonistic actuator on a racket for experiment.
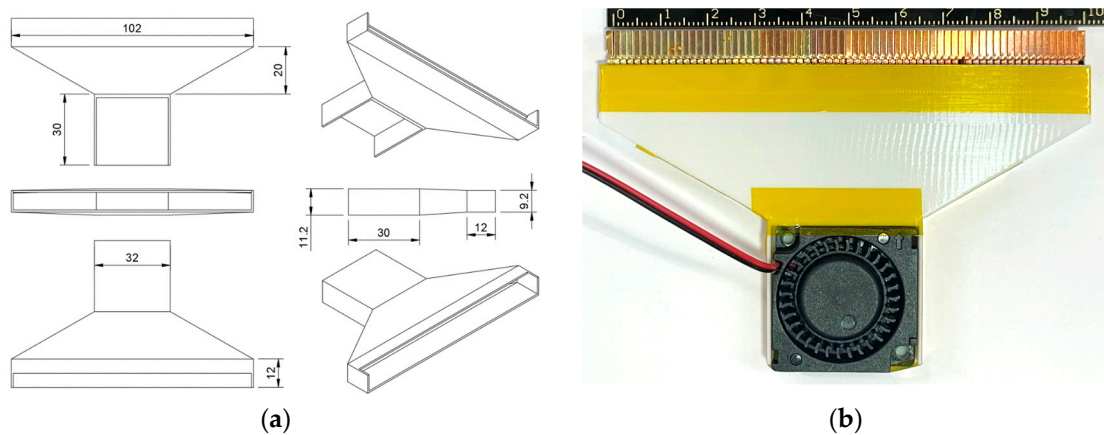

Figure 11. The 3D-printed air deflector: (**a**) Detailed dimensions of the deflector (mm); (**b**) an assembled copper cooling sink with air deflector and centrifugal fan.

4. Sensing and Controlling Methodology

This section describes the sensing and control circuits and algorithms used. PC-based communication is used to unify the control and sensing system and reduce complexity. A refined multi-processed PID controller increases the detection and control rate.

4.1. Controlling and Sensoing Circuits

To acquire an actuate measuring of the actuator state and drive the SMA actuator, sensors and drivers are required. A USB-based protocol approach simplifies the reporting and updating process. As shown in Figure 12a, an FT232H USB bridging chip from FTDI Co. provides an inter-integrated circuit (I2C) port via a USB-to-PC connection. FT232H provides one channel of I2C fast-mode connection, operating at 1 MHz to connect sensors or amplifiers.
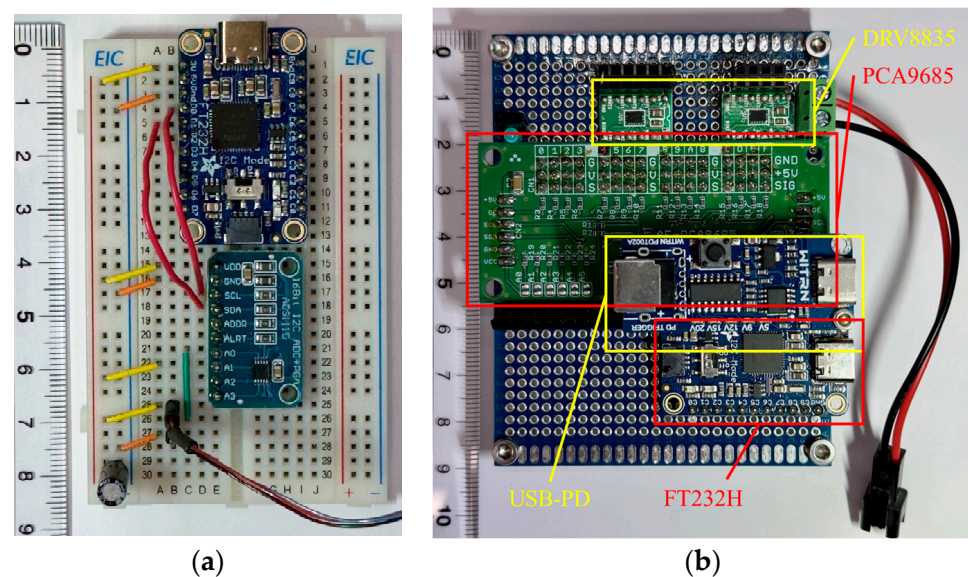

(a)   (b)

Figure 12. The sensor and driver circuits: (**a**) FT232H and ADS1115 circuit for signal encoding; (**b**) the powering circuit for the SMA actuator.

The direct control of an SMA actuator is achieved using temperature. A viable method of predicting future SMA length deflection involves assessing the real-time temperature distribution along the wire's longitudinal direction. Common methods of doing so involve acquiring this distribution using an array of infrared cameras. However, existing infrared camera sensor modules usually report a low frequency of less than 20 Hz. Also, it is difficult to predict non-linear relations among current deflection, temperature, tension, and future deflection. Thus, the deflection angle is directly encoded into feedback signals to avoid thermal information.

As shown in Figure 10, an HW-526 rotary resistor connects two sides of the actuator through an eccentric shaft shown in Figure 8. Following the rotation of the motion side, HW-526 converts the rotation into electric potential. The ADS1115 analog-to-digital converter (ADC) encodes the potential value and reports to FT232H through a dedicated I2C channel. ADS1115 converts and saves the potential in two 8-bit registers using 2's complement integer data with a speed of 860 samples per second. ADS1115 reports to the controller program at a frequency of approximately 1200 Hz. A former conversion result is reported if the latest cycle is ongoing. Figure 12a shows connected circuits. A 3.3 V voltage powers the HW-526 and ADS1115 since the ADC exhibits lower reading variation compared to 5 V. A 0.22 μF electrolytic capacitor is used to reduce noise on 3.3 V powering. HW-526 provides resistance variation from 0 to 10.9 KΩ, corresponding to 0 to 333.3 degrees of

rotation, with a linearity of $\pm 2\%$. A linear model calculates the received integer data into real-time deflection angle θ_t:

$$\theta_t = kD_t + b \tag{3}$$

where D_t represents the received data decoded from a 16-bit register, and k and b are parameters of the linear model. The actuator is turned to $-90°$ and $+90°$ deflection angles for calibration of the sensor, which results in $k = 0.013078$, and $b = 171.21$.

　　　The SMA wire needs to be powered with an adjustable electric power for the purpose of control. Pulse width modulation (PWM) is one of the effective methods for adjusting the equivalent voltage. As shown in Figure 12b, a PCA9685 driver chip generates PWM signals following I2C commands. With 16 PWM output channels, a PCA9685 provides adjustable duty ratios of 4096 steps (12-bit) while permitting frequency adjustments up to 1526 Hz. The maximum output current for each channel is around 25 mA at 5 V. To compensate for this, DRV8835 double H-bridge ICs are employed to amplify the output signal. Each DRV8835 has two individual H-bridges controlled by built-in MOSFETs, providing up to 1.5 A of current under 9 V. In this study, a 100 W USB-PD to DC converter module provides a 9 V power supply for the amplifier, as shown in Figure 12b. The PWM wave for the centrifugal fan is provided by PCA9685, following the same control and amplification circuit as the SMA wire. The fan's maximum duty ratio is 50% in order to prevent damage.

4.2. Controlling Methodology

　　　The SMA-based actuator principally operates through length deflection caused by temperature change induced by electrical Joule heating. During operation, the angular deflection of the actuator joint exhibits non-linearity in relation to the applied electric powering, which makes it hard to predict.

　　　Taking the SMA wire as an object of control, aiming for better control performance, negative feedback control is employed within a closed-loop control system. The sensor signal is fed back, compared with inputs for an error signal, and utilized for control purposes with the aim of reducing or eliminating deviations. Consequently, the PID controlling method controls the actuator in order to reach the target trajectory.

　　　As shown in Figure 13, the proposed control system consists of two inputs: The desired angle and the current angle decoded from a sensor. The controller will generate command signals based on the deviation of two angles in order to adjust the PWM duty ratio. The PWM signal, in turn, affects the temperature of the SMA wire and adjusts the duty cycle, influencing temperature change speed, thus affecting the contraction and relaxation progress of SMA wire length, forcing the mechanical structure to move, and resulting in a change in joint angle. When the deflection angle is less than desired, the controller will increase the duty ratio to raise the wire temperature and cause the SMA wire to contract. Conversely, when the angle exceeds the desired angle, the controller reduces the PWM duty cycle to a lower temperature and relaxes the SMA wire.
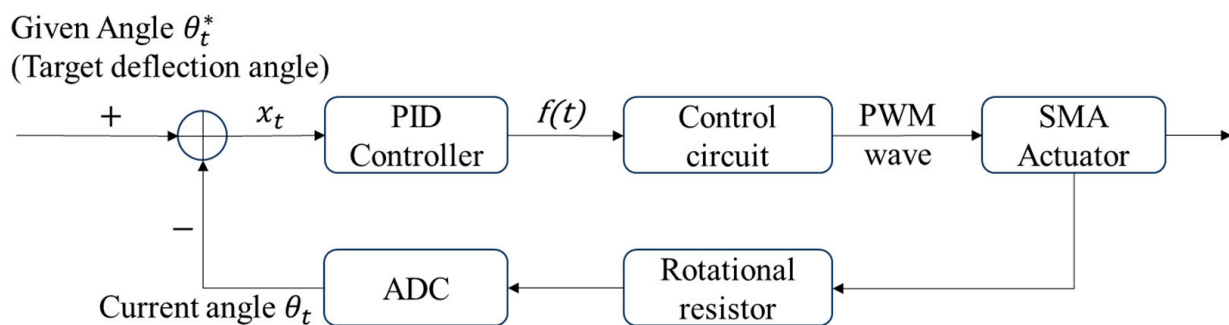

Figure 13. Block diagram of the proposed system with PID control.

The control equation for the PID controller is as follows:

$$f(t) = K_p\, x_t + K_i \int_0^t x_t\, dt + K_d \frac{dx_t}{dt} \tag{4}$$

where K_p represents the proportional control parameter, K_i represents the integral control parameter, and K_d represents the derivative control parameter. As indicated in Figure 13, the input of the system is the error of deflection, denoted as $x_t = \theta_t^* - \theta_t$, where θ_t^* and θ_t represent the current target deflection angle and the current deflection angle, respectively. Applying calculations in the formula feeds an output control signal (PWM wave duty ratio) into the controlled process. In PID control, K_p influences steady-state error and response speed. K_i operates in the low-frequency range of the system's frequency characteristics, reducing steady-state error. K_d introduces early corrective signals based on the trend of the input signal, reducing overshoot and improving system stability. By combining characteristics of proportional, integral, and derivative control and selecting appropriate parameters, the strengths of each component can be leveraged. PID may effectively control SMA length, subsequently enabling the control system to achieve desired finger angles.

The PID controller shares a dedicated sub-process, while the sensor program shares another. Each process controls one dedicated I2C channel for a higher communication frequency, avoiding frequent waiting for I2C handshaking.

5. Evaluation and Discussion

In this section, the performance of the proposed actuator cooling design is evaluated through controlled experiments and discussed via comparison with the existing design.

5.1. Relaxation Evaluation by Single Wire Actuator

A performance criterion is needed to measure the SMA-tendon-driven actuator's performance accurately. In most studies, it has been observed that, during the actuation–sustainment–relaxation cycle, actuation lasts for less than 0.5 s, while relaxation takes significantly longer. Typically, relaxation lasts for more than 2 s, with some such periods lasting for over 20 s. The duration of relaxation significantly impacts overall performance. Therefore, evaluating actuators by measuring the relaxation duration under controlled conditions is essential.

The actuator of each cooling solution is tested for flexor and extensor configurations. The flexor-configured actuator has a deflection angle of $\theta > 0$, and the extensor actuator has a $\theta < 0$, as illustrated in Figure 3. In both cases, a stand holds a single-wired actuator horizontally and the extension force can be given by a 20 g weight, as shown in Figure 9.

The SMA wire is excited during the first 2 s with a 9V PWM power supply in both scenarios, using a 40% duty ratio. Then, the driving board outputs 0% PWM for relaxation. The sensor reading subprocess records data for 20 s, leaving enough time for relaxation. Pretesting shows the existence of a 0.3 s delay for the start of the control subprocess due to I2C bus handshaking and slave chip initializing. For a complete recording of experiments, the sensor reading subprocess starts 0.6 s before the actuation subprocess starts. Consequently, the activation and relaxation stages commence at 0.9 s and 2.9 s, respectively. During both tests, the ADC chip samples the rotary resistor at around 860 Hz and reports to the hosting PC at approximately 1200 Hz in a dedicated sampling subprocess. Reported data include the decoded deflection angle θ_t and a timestamp t.

Figures 14–17 show the performance of differently configured actuators, where SMA stands for exposed SMA wire, TSMA indicates Teflon capillary-only wrapped SMA wire, and CTSMA presents copper- and Teflon-wrapped actuators. HSSMA stands for an SMA wire applied with a heat sink without powering centrifugal fans. During the test, the centrifugal fan keeps running at the maximum duty ratio in order to test the relaxation performance at full potential. Figures 14 and 15 show recorded raw data from flexor and extensor experiments, while Figures 16 and 17 illustrate smoothed velocity calculated from deflection recordings.
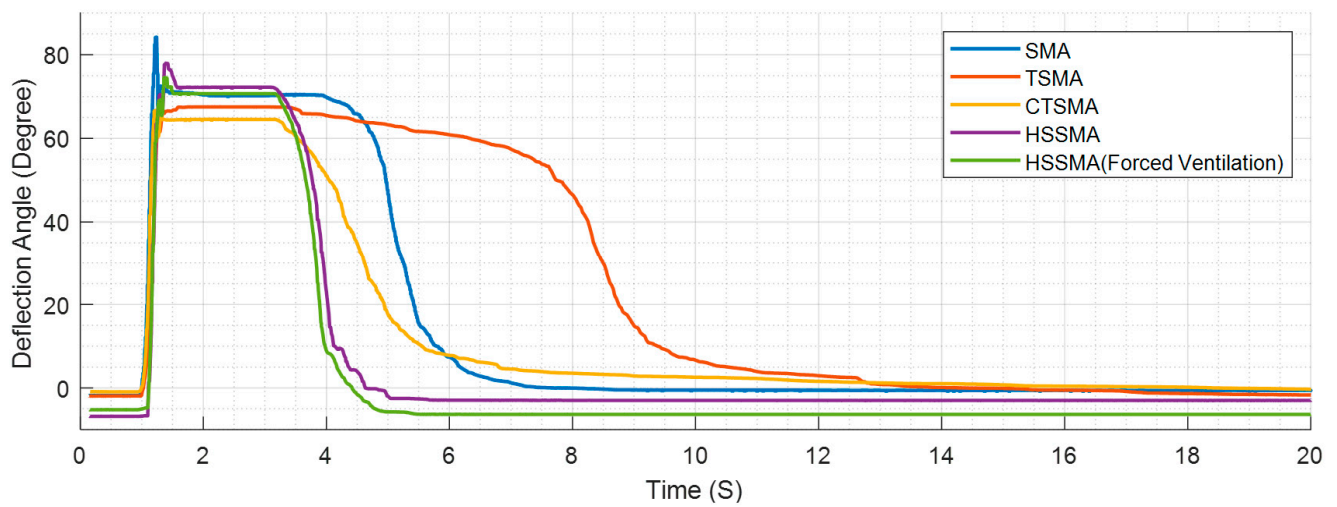
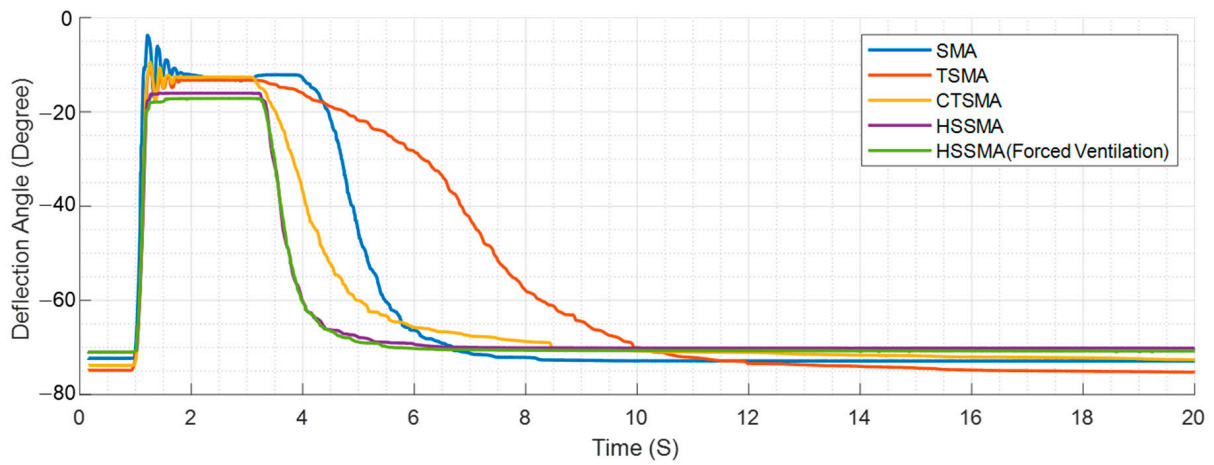**Figure 14.** Deflection reading of flexor side during activation and relaxation.

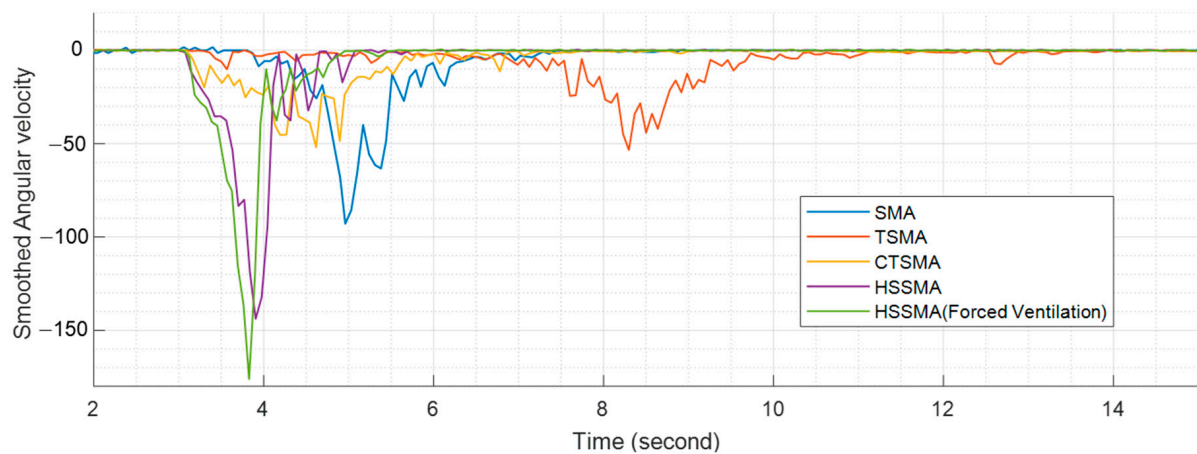**Figure 15.** Deflection reading of extensor side during activation and relaxation.

Figure 16. Angular velocity (smoothed) of flexor side during relaxation.
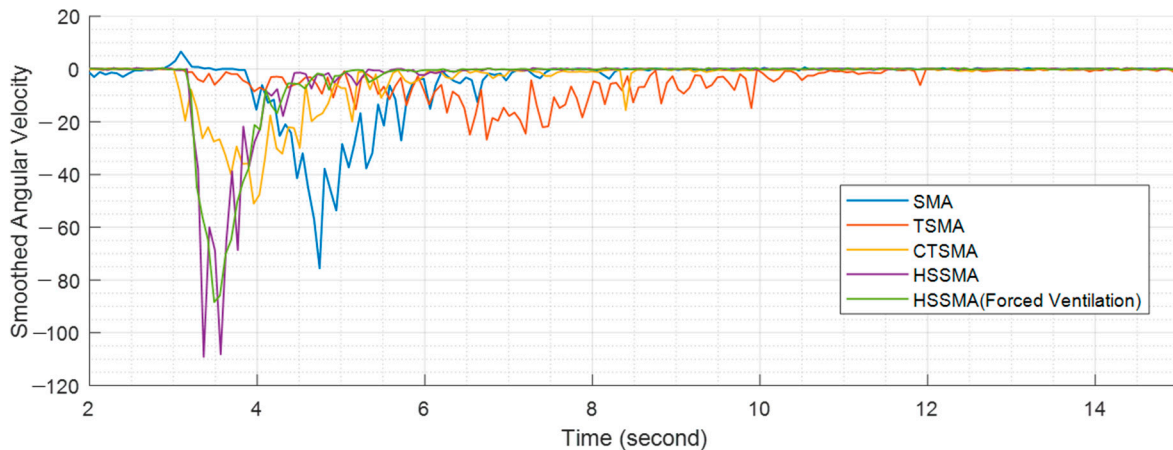
Figure 17. Angular velocity (smoothed) of extensor side during relaxation.

Figures 14 and 15 show the typical actuating–sustaining–relaxing cycle of the flexor and extensor actuator when activated by an equivalent sustaining DC voltage. Figures 16 and 17 show the calculated and smoothed (windows size 120) angular rate. It is simple to categorize working states into initial, impacting, sustaining, relaxing, and static. Both figures show that actuators with heatsink perform better than SMA, TSMA, and CTSMA actuators, settling significantly earlier.

Compared to exposed SMA, which has direct contact with the surrounding air, the existence of the Teflon layer significantly slowed down the heat-transferring process, compelling the TSMA actuator to react several seconds later than the point of powering off. Meanwhile, the CTSMA actuator curve cooled significantly faster than TSMA, but showed minimal improvement compared to the exposed SMA actuator.

All test results show that SMA-driven actuators undergo a non-linear descending process during the relaxation stage. Figures 16 and 17 show that relaxation speed follows a near-symmetrical bell-shaped curve. The descent reaches a maximum speed approximately halfway through the relaxation duration; this is followed by a period with a longer-term, slower-descending speed.

However, considering that each manufactured SMA actuator possesses variance in initial length and aging state, an accurate measurement method accounting for the relaxing stage is required to compensate for influence and thus obtain a more precise comparison. To account for such factors, the relaxation percentage d_{relax} is calculated as:

$$d_{elax} = \frac{d_t}{d_{full}} \times 100\% \tag{5}$$

where $d_t = \theta_t - \theta_0$ is the current deflection angle and $d_{full} = \theta_{max} - \theta_0$ is the range of deflection. For different actuator configurations, comparing time consumed for the same length of time d_{relax} will mitigate the influence of varying SMA wire lengths.

Tables 3 and 4 show the deflection range of different actuators, configured either as a flexor or an extensor tendon. The initial deflection θ_0 is calculated by averaging the sensor reading from 0.2 s to 0.8 s, where the 40% duty ratio activation starts at 0.9 s. Before the recording process starts, θ_0 is adjusted to be as accurate as possible using the adjusting gear shown in Figure 9.

To avoid disturbances from the impact caused by fast actuation, the maximum sustainable deflection angle θ_{max} is calculated by averaging between 2.5 s and 2.8 s, where the fast activation is finished. During such a process, the actuator is kept stable by 40% sustained power. The final deflection angle θ_{end} is calculated by averaging the results from 19 s to 20 s to show an achievable long-term final relaxation. The deflection range is calculated using the formula $\theta_{max} - \theta_0$, and the relaxation range is calculated by $\theta_{max} - \theta_{end}$.

Table 3. Flexor-side deflection range of the single-joint SMA actuators.

Angle	SMA	TSMA	CTSMA	HSSMA Passive	HSSMA Forced Ventilation
Initial Deflection (at 0 S)	−1.841	−1.948	−0.936	−6.829	−5.248
Maximum Deflection	70.204	67.522	64.536	72.236	70.704
Final Deflection (at 20 S)	−0.608	−1.635	−0.220	−3.021	−6.370
Deflection Range	72.045	69.470	65.472	79.065	75.952
Relaxation Range	70.812	69.157	64.756	75.257	77.073

Table 4. Extensor-side deflection range of the single-joint SMA actuators.

Angle	SMA	TSMA	CTSMA	HSSMA Passive	HSSMA Forced Ventilation
Initial Deflection (at 0 S)	−72.298	−74.835	−73.795	−71.008	−71.003
Maximum Deflection	−13.207	−13.265	−12.619	−16.027	−17.146
Final Deflection (at 20 S)	−72.866	−75.188	−72.532	−70.138	−70.764
Deflection Range	59.091	61.571	61.177	54.981	53.857
Relaxation Range	59.659	61.923	59.913	54.111	53.619

The deflection range d_{full} allows researchers to measure performance without interference from the assembling of the actuator. The timestamp that each actuator first relaxed to d_{relax} is recognized from recorded experiment data and shown in Figures 18 and 19.
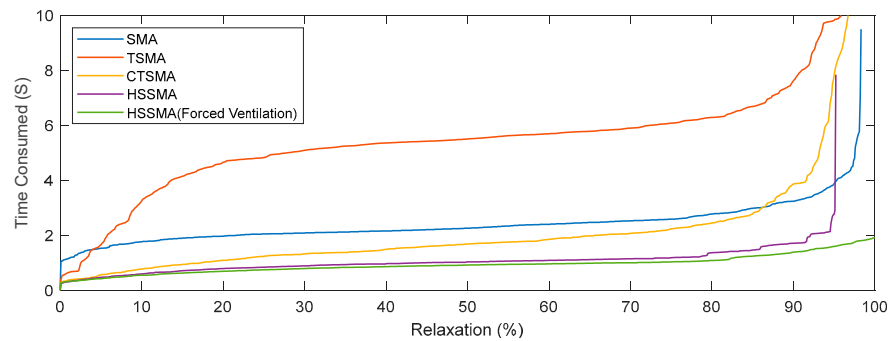

Figure 18. Time consumed to attain relaxation state (Flexor side).
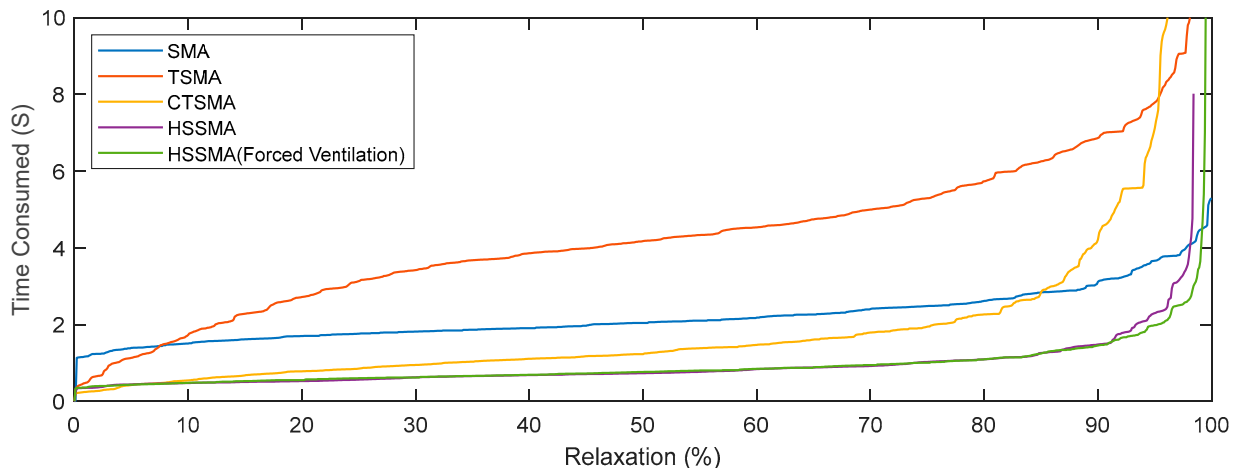

Figure 19. Time consumed to attain relaxation state (Extensor side).

The figures show that some configurations require additional time for the first 1% of relaxation, especially the SMA actuator. Considering all actuators are heated by a 40%, 9 V PWM wave, a possible reason for this additional time is that actuators are overheated during the actuating–sustaining stage, caused by their relatively smaller thermal mass. Overheating increases the wire temperature before the relaxation stage begins, driving the process longer than required. Additionally, some tests cannot finish the final 5% relaxation within 20 s of the experiment. Compensating for these factors, performance is compared on the basis of the temporal duration from 1% to 95% relaxation. As shown in Tables A1 and A2 in Appendix B, the timestamp at which d_{relax} values are first achieved during the relaxation process is used to perform comparisons.

Table 5 shows experimental results. On the flexor side, TSMA, CTSMA, HSSMA, and HSSMA with forced convection consumed 337%, 274%, 90%, and 46% of the time compared to the exposed SMA actuator. On the extensor side, actuators take 292%, 275%, 78%, and 65% of the time consumed by the exposed SMA actuator, respectively.

Table 5. Time (s) consumed for relaxation of 1% to 95% angle range.

Relaxation Performance	SMA	TSMA	CTSMA	HSSMA Passive	HSSMA Forced Convection
Flexor side	2.720	9.179	7.454	2.456	1.269
Extensor side	2.497	7.308	6.877	1.949	1.624

For embedded robotic applications, being wrapped in Teflon provides electric insulation but extends the relaxation time by approximately threefold. Introducing a copper tube around the Teflon capillary improves TSMA performance by 10% to 20%, compensating for the low thermal conductivity of Teflon material by providing an increased air-contacting area. Still, TSMA and CTSMA actuators suffer from slow relaxation.

The HSSMA actuator, which employs a welded heat sink, performs significantly better than TSMA and CTSMA, consuming less than one-third of the time and fully compensating for the existing Teflon capillary. Furthermore, with the activation of two centrifugal fans, the HSSMA actuator requires only half the time compared to the SMA actuator on the flexor side and 65% compared to the extensor side, demonstrating a significantly enhanced relaxing performance.

5.2. Responding Performance

Both responding and signal tracking performances are evaluated to show the responding performance of the agonistic–antagonistic actuator described in Section 3.2. In order to avoid the influence of gravity, the actuators are placed vertically, as shown in Figure 10b.

During the test, a duty ratio range of $[-50, 50]$% limits the PWM output, which is mapped to the $[-1, 1]$ range of the PID output. The limitation prevents the SMA wire from breaking due to large tension when a rapid input change occurs.

For a PID signal output $f(t) \in (0, 1]$, the flexor-side SMA wire will receive a duty ratio of $f(t)$, the extensor-side SMA wire will be powered off, and the extensor fan will be powered at the maximum duty ratio. When $f(t) \in [-1, 0)$, extensor SMA receives a duty ratio of $-f(t)$, flexor power will be powered off, and the flexor fan will be set at the maximum duty ratio. When output $f(t) = 0$, both fans will be turned on while both wires will be powered off.

Figure 20 shows the actuator trajectory when following a 0-degree constant deflection target. Initially, the actuator is set to minimum deflection at $\theta_0 = -57.3°$, which is limited physically by the structures on the opposite side. The PID controller will activate and stabilize the joint to the target deflection angle $\theta_t^* = 0°$, with fine-tuned PID parameters of K_p, K_i, and K_d of $(160, 40, 4)$, at a 60 Hz update frequency.
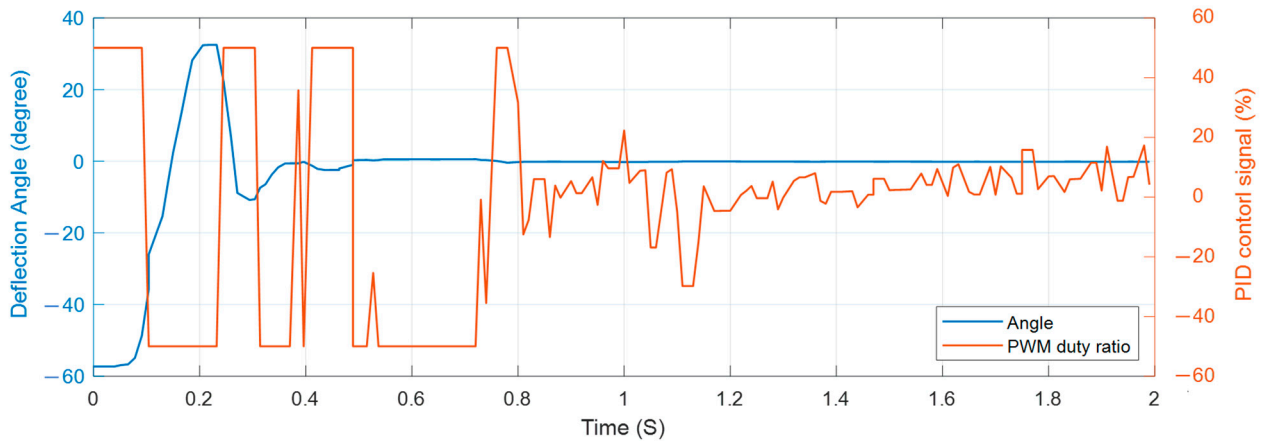
Figure 20. Deflection angle curve and control signal under PID control.

The results show a 56.72% overshoot. It can be seen that the system stabilized at 0.48 s with a variation of less than 0.82% in terms of range and at 0.8 s for 0.24% variation. The results indicate that the proposed device performs better when attaining a targeted deflection angle.

A sine wave-tracking task evaluates the proposed actuator. Figure 21 shows a trajectory following a sine wave of a 0.2 Hz frequency and a 20 degree amplitude. The same PID control is used with a fine-tuned parameter K_p, K_i, and K_d of $(6.2, 8, 1)$. The recorded sensor data show that the actuator starts with a fast motion and a large overshoot of $-28.5°$ deflection while the target is $11.1°$. Soon, the actuator reached a more stable tracking of the input wave at only 0.29 s after activation started. With PID control, the proposed design has a root-mean-square error $RMSE = 4.16$ over the entire tracking duration, and an $RMSE = 2.90$ when excluding early-stage overshoot. The results indicate that the proposed methods exhibit robust responsiveness for a stable target position within 0.5 s and can accurately track a varying signal with a confined margin of error.
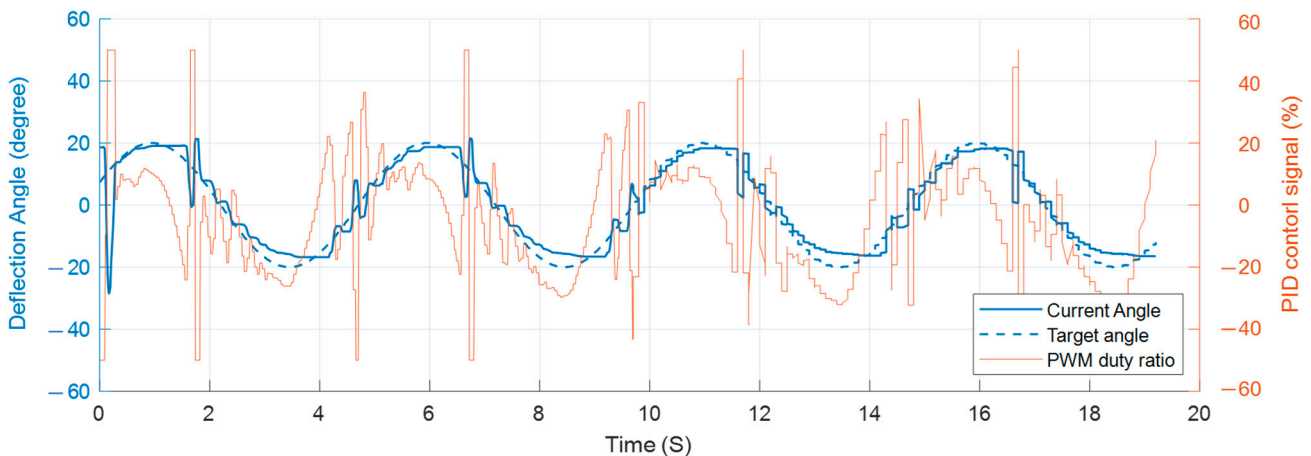

Figure 21. The trajectory of the proposed antagonistic pair SMA actuator in sine wave tracking.

Considering the tracking of a sine wave of higher frequency, the adjustment value for the next time step is based on the existing angle, which causes SMA wires on two sides to be heated alternatively. Such behavior significantly decreases the time window for the opposite relaxation and damages the motion range. Tests show that tracking a 0.5 Hz sine wave will cause the activation amplitude to be reduced to $\pm10°$, and will eventually cause the stretching of both wires, leading to a rupture, as shown in Figure 22.
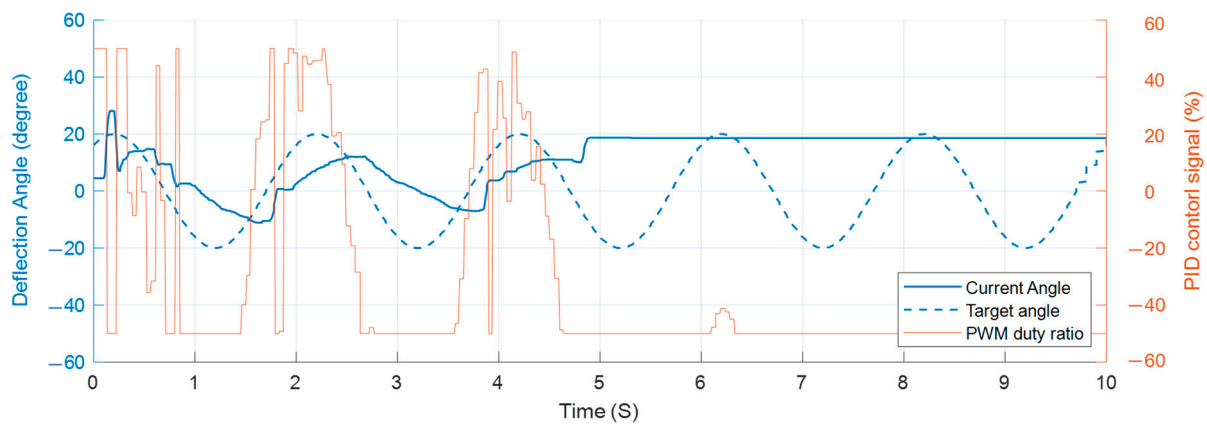
Figure 22. A 0.5 Hz sine wave tracking result of the proposed actuator.

Compared to the high responsiveness that the proposed actuator demonstrated in tracking a static angle, its performance in dynamic tracking is unsatisfactory. When the actuator tries to correct from an overshoot, the reversed wire is heated with a lower amplitude while the relaxing wire undergoes the relaxing process. This situation repeatedly occurs during the tracking task, constantly causing the antagonistic wire pair to produce counteractive forces frequently. The proposed SMA actuator offers a better performance in terms of maintaining a target angle than its capacity to follow a rapidly changing target.

5.3. Discussion

The proposed device enhanced the relaxation performance of the multi-layered wrapping SMA actuator, improving responsiveness and reducing latency between working cycles. Meanwhile, introducing the heat sink, deflector, and fan increased the size and weight of the system compared with TEC or liquid-cooling actuators.

However, the system size and weight were still larger than those of an exposed SMA actuator, limiting the application for small and dense targets, such as composite structures that embed the SMA wires into fabric or jelly-like materials. The design can provide internal tension via extension. With a designed positioner, the interior wire can provide tension, while the exterior wire with the proposed cooling design provides length deflection. Although the design can be used in such scenarios, the compactness and lightweight will be compromised.

Compared to traditional methods, the direct driving from the SMA wire can be extended into tight spaces, making the proposed actuator suitable for applications in biomimicry systems that require linear or rotational motion, such as robotic fingers and arms.

The servo motors applied in those scenarios usually consider proximal and distal driving methods. The application of a proximal driving motor through finger joints exhibits limitations related to motor size, resulting in a small output force. Distal driving motors are commonly connected to the finger joint, with tendons placed in the forearm. The motors for complex biomimicry fingers with a higher degree of freedom are arranged inside human-size forearms, occupying a large amount of space. For each side of a robotic hand, proposed cooling designs can be shared by welding multiple wrapped SMA wires onto one heatsink. This can significantly reduce the required space and weight and improve the overall power ratio. The ratio of wires to heatsinks can be increased until the relaxation speed reduces significantly.

On the other hand, the used electrical circuits are handmade on breadboards. Using PCBs can significantly reduce the size and weight of the board. Nevertheless, electric-driven approaches still require heavy and oversized batteries when employed in mobile robots, which remains a limitation.

The classical PID method can provide basic control for the actuator. Due to the heat-driving nature of SMA material, difficulty in control persists. When systemic complexity

increases, or more precise motions are required, control becomes harder. Thus, methods based on artificial neural networks, such as deep reinforcement learning and inverse learning, are potential methods to obtain better control.

6. Conclusions

In this paper, the thermal performance of SMA-tendon-driven soft actuators is explored. A novel cooling design using small form-factor copper fin heat sinks and centrifugal fans is proposed based on a multi-layer wrapped SMA strategy. Prototype devices are built to show the performance of the design. An electronic system is refined for an accurate evaluation, achieving a higher data rate for sensors and actuators. Experiments on relaxation speed are presented, illustrating that the proposed design outperforms previous research by consuming 54% less than an exposed SMA wire and performing up to 5.8 times better than a multi-layer wrapped SMA actuator. In the future, advancing control methods can be pursued to achieve more precise and adaptive movement control.
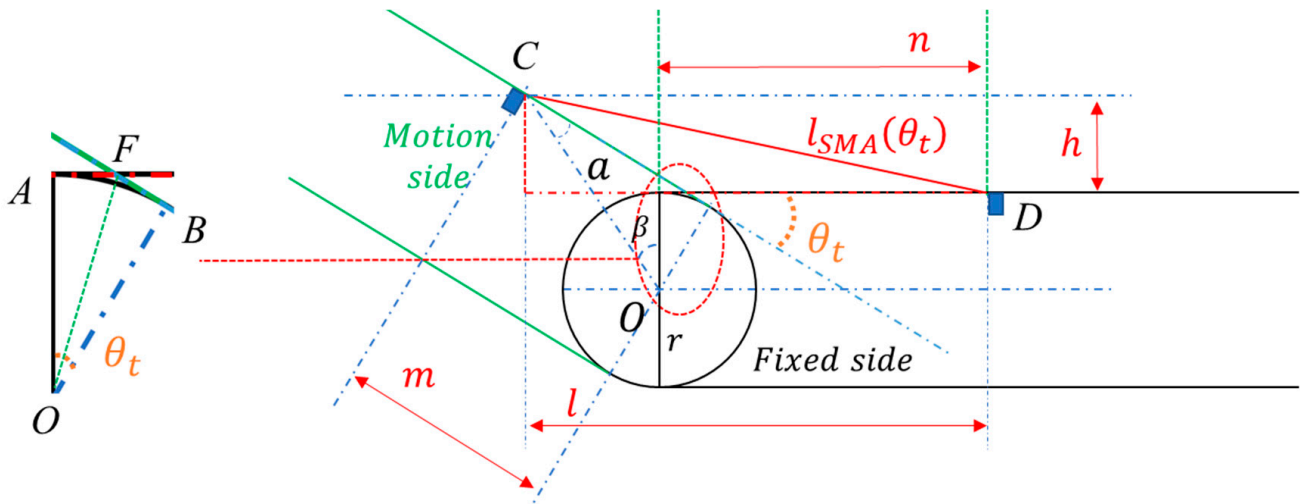
Appendix A

Figure A1. Illustration of a flexor configured SMA tendon actuator.

Let $l_{SMA} = CD$, it is easy to know:

$$AF = BF = r * \tan \frac{\theta_t}{2} \tag{A1}$$

From the Law of Cosines:

$$l_{SMA}{}^2 = CF^2 + DF^2 - 2CF * DF * \cos(\pi - \theta_t)$$
$$= \left(m - r * \tan \tfrac{\theta_t}{2}\right)^2 + \left(n - r * \tan \tfrac{\theta_t}{2}\right)^2 - 2*\left(m - r * \tan \tfrac{\theta_t}{2}\right) * \left(n - r * \tan \tfrac{\theta_t}{2}\right) * \cos(\pi - \theta_t)$$
$$= \left(m - r * \tan \tfrac{\theta_t}{2}\right)^2 + \left(n - r * \tan \tfrac{\theta_t}{2}\right)^2 + 2*\left(m - r * \tan \tfrac{\theta_t}{2}\right) * \left(n - r * \tan \tfrac{\theta_t}{2}\right) * \cos\theta_t$$
$$= m^2 + n^2 - 2*(m+n)r * \tan \tfrac{\theta_t}{2}(1 + \cos \theta_t) + 2r^2\tan^2 \tfrac{\theta_t}{2}(1 + \cos \theta_t) + 2mn\cos \theta_t \tag{A2}$$
$$l_{SMA}{}^2 = \left(m - r * \tan \tfrac{\theta_t}{2}\right)^2 + \left(n - r * \tan \tfrac{\theta_t}{2}\right)^2 - 2*\left(m - r * \tan \tfrac{\theta_t}{2}\right) * \left(n - r * \tan \tfrac{\theta_t}{2}\right) * \cos(\pi - \theta_t)$$
$$= \left(m - r * \tan \tfrac{\theta_t}{2}\right)^2 + \left(n - r * \tan \tfrac{\theta_t}{2}\right)^2 + 2*\left(m - r * \tan \tfrac{\theta_t}{2}\right) * \left(n - r * \tan \tfrac{\theta_t}{2}\right) * \cos\theta_t$$
$$= m^2 + n^2 - 2*(m+n)r * \tan \tfrac{\theta_t}{2}(1 + \cos \theta_t) + 2r^2\tan^2 \tfrac{\theta_t}{2}(1 + \cos \theta_t) + 2mn\cos \theta_t$$

While $\theta_t \in (0, \pi)$:

$$\tan^2 \frac{\theta_t}{2} = \frac{1 - \cos \theta_t}{1 + \cos \theta_t} = \frac{\sin^2 \theta_t}{\left(1 + \cos \theta_t\right)^2} \tag{A3}$$

Considering $\sin \theta_t > 0$ and $\cos \theta_t > -1$:

$$\tan \frac{\theta_t}{2} = \frac{\sin \theta_t}{(1 + \cos \theta_t)} \tag{A4}$$

So:

$$l_{SMA}{}^2 = m^2 + n^2 - 2*(m+n)r * \tan \tfrac{\theta_t}{2}(1 + \cos \theta_t) + 2r^2\tan^2 \tfrac{\theta_t}{2}(1 + \cos \theta_t) + 2mn\cos \theta_t$$
$$= m^2 + n^2 - 2(m+n)r \tfrac{\sin \theta_t}{(1+\cos \theta_t)}(1 + \cos \theta_t) + 2r^2 \tfrac{1-\cos \theta_t}{1+\cos \theta_t}(1 + \cos \theta_t) + 2mn\cos \theta_t$$
$$= m^2 + n^2 - 2(m+n)r\sin \theta_t + 2r^2(1 - \cos \theta_t) + 2mn\cos \theta_t$$
$$= m^2 + n^2 + 2r^2 - 2(m+n)r\sin \theta_t + \left(2mn - 2r^2\right)\cos \theta_t \tag{A5}$$

Thus:

$$l_{SMA} = \sqrt{m^2 + n^2 + 2r^2 - 2(m+n)r\sin \theta_t + (2mn - 2r^2)\cos \theta_t}, \ \theta_t \in (0, \pi) \tag{A6}$$

Considering $\theta_t = 0$, obviously

$$l_{SMA} = m + n = \sqrt{m^2 + n^2 + 2r^2 - 2(m+n)r\sin 0 + (2mn - 2r^2)\cos 0} \tag{A7}$$

Finally:

$$l_{SMA} = \sqrt{m^2 + n^2 + 2r^2 - 2(m+n)r\sin \theta_t + (2mn - 2r^2)\cos \theta_t}, \ \theta_t \in [0, \pi) \tag{A8}$$

Appendix B

Table A1. Time of relaxation reached during the relaxation stage (Flexor side).

Relaxation Percentage * (Degree)	SMA (Second)	TSMA (Second)	CTSMA (Second)	HSSMA Passive (Second)	HSSMA Forced Ventilation (Second)
0	0.100	0.005	0.013	0.002	0.001
1	1.160	0.643	0.370	0.310	0.325
5	1.530	1.658	0.563	0.469	0.422
10	1.760	3.248	0.773	0.593	0.545
25	2.050	4.828	1.229	0.840	0.748
50	2.260	5.505	1.685	1.032	0.918
75	2.590	6.081	2.236	1.184	1.031
90	3.240	7.627	3.865	1.711	1.388
95	3.880	9.822	7.825	2.766	1.594

Table A1. *Cont.*

Relaxation Percentage * (Degree)	SMA (Second)	TSMA (Second)	CTSMA (Second)	HSSMA Passive (Second)	HSSMA Forced Ventilation (Second)
99	--	14.644	16.729	--	1.842
100	--	--	--	--	1.925

* Relaxation Percentage: d_{relax}; --: Angle unachieved during test.

Table A2. Time of Relaxation reached during the relaxation stage (Extensor side).

Relaxation Percentage * (Degree)	SMA (Second)	TSMA (Second)	CTSMA (Second)	HSSMA Passive (Second)	HSSMA Forced Ventilation (Second)
0	0.005	0.002	0.003	0.001	0.001
1	1.168	0.482	0.245	0.349	0.361
5	1.392	1.131	0.422	0.438	0.431
10	1.504	1.730	0.543	0.476	0.481
25	1.763	3.131	0.851	0.564	0.603
50	2.044	4.177	1.230	0.733	0.765
75	2.484	5.292	1.945	1.026	1.003
90	3.114	6.863	4.216	1.481	1.455
95	3.666	7.790	7.123	2.298	1.985
99	4.472	11.788	--	--	3.650
100	5.291	13.284	--	--	--

* Relaxation Percentage: d_{relax}; --: Angle unachieved during test.

References

1. Ölander, A. An Electrochemical Investigation of Solid Cadmium-Gold Alloys. *J. Am. Chem. Soc.* **1932**, *54*, 3819–3833. [CrossRef]
2. Tanaka, K.; Kobayashi, S.; Sato, Y. Thermomechanics of transformation pseudoelasticity and shape memory effect in alloys. *Int. J. Plast.* **1986**, *2*, 59–72. [CrossRef]
3. Furuya, Y.; Shimada, H. Shape memory actuators for robotic applications. *Mater. Des.* **1991**, *12*, 21–28. [CrossRef]
4. Chang-Jun, Q.; Pei-Sun, M.; Qin, Y. A prototype micro-wheeled-robot using SMA actuator. *Sens. Actuators A Phys.* **2004**, *113*, 94–99. [CrossRef]
5. Veeramani, A.S.; Buckner, G.D.; Owen, S.B.; Cook, R.C.; Bolotin, G. Modeling the dynamic behavior of a shape memory alloy actuated catheter. *Smart Mater. Struct.* **2008**, *17*, 015037. [CrossRef]
6. Singh, K.; Sirohi, J.; Chopra, I. An Improved Shape Memory Alloy Actuator for Rotor Blade Tracking. *J. Intell. Mater. Syst. Struct.* **2003**, *14*, 767–786. [CrossRef]
7. Karakalas, A.A.; Machairas, T.T.; Saravanos, D.A. Effect of shape memory alloys partial transformation on the response of morphing structures encompassing shape memory alloy wire actuators. *J. Intell. Mater. Syst. Struct.* **2019**, *30*, 1682–1698. [CrossRef]
8. Benafan, O.; Moholt, M.R.; Bass, M.; Mabe, J.H.; Nicholson, D.E.; Calkins, F.T. Recent Advancements in Rotary Shape Memory Alloy Actuators for Aeronautics. *Shap. Mem. Superelasticity* **2019**, *5*, 415–428. [CrossRef]
9. Bishay, P.L.; Finden, R.; Recinos, S.; Alas, C.; Lopez, E.; Aslanpour, D.; Flores, D.; Gonzalez, E. Development of an SMA-based camber morphing UAV tail core design. *Smart Mater. Struct.* **2019**, *28*, 075024. [CrossRef]
10. Bishay, P.L.; Aguilar, C.; Amirbekyan, A.; Vartanian, K.; Arjon-Ramirez, M.; Pucio, D. Design of a lightweight shape memory alloy stroke-amplification and locking system in a transradial prosthetic arm. In *2021 ASME Conference on Smart Materials, Adaptive Structures and Intelligent Systems (SMASIS) Proceedings*; SMASIS2021-68248, V001T05A015; ASME: New York, NY, USA, 2021. [CrossRef]
11. Andrianesis Tzes, A. Development and Control of a Multifunctional Prosthetic Hand with Shape Memory Alloy Actuators. *J. Intell. Robot Syst.* **2015**, *78*, 257–289. [CrossRef]
12. Soriano-Heras, E.; Blaya-Haro, F.; Molino, C.; de Agustín del Burgo, J.M. Rapid prototyping prosthetic hand acting by a low-cost shape-memory-alloy actuator. *J. Artif. Organs.* **2018**, *21*, 238–246. [CrossRef] [PubMed]
13. Bishay, P.L.; Fontana, J.; Raquipiso, B.; Rodriguez, J.; Borreta, M.J.; Enos, B.; Gay, T.; Mauricio, K. Development of a biomimetic transradial prosthetic arm with shape memory alloy muscle wires. *Eng. Res. Express* **2020**, *2*, 035041. [CrossRef]
14. Bundhoo, V.; Haslam, E.; Birch, B.; Park, E.J. A shape memory alloy-based tendon-driven actuation system for biomimetic artificial fingers, part I: Design and evaluation. *Robotica* **2009**, *27*, 131–146. [CrossRef]
15. Gilardi, G.; Haslam, E.; Bundhoo, V.; Park, E.J. A shape memory alloy based tendon-driven actuation system for biomimetic artificial fingers, part II: Modelling and control. *Robotica* **2010**, *28*, 675–687. [CrossRef]

16. Cheng, S.S.; Kim, Y.; Desai, J.P. Modeling and characterization of shape memory alloy springs with water cooling strategy in a neurosurgical robot. *J. Intell. Mater. Syst. Struct.* **2017**, *28*, 2167–2183. [CrossRef] [PubMed]
17. Park, S.J.; Choi, K.; Rodrigue, H.; Park, C.H. Soft Exosuit Based on Fabric Muscle for Upper Limb Assistance. *IEEE/ASME Trans. Mechatron.* **2023**, *28*, 26–37. [CrossRef]
18. Park, S.J.; Choi, K.; Rodrigue, H.; Park, C.H. Fabric muscle with a cooling acceleration structure for upper limb assistance soft exosuits. *Sci. Rep.* **2022**, *12*, 11398. [CrossRef]
19. Liu, R.; Sawada, H. An SMA Wire-based Tendon Actuator and its Application on Robotic Fingers. In Proceedings of the 2023 IEEE International Conference on Mechatronics and Automation (ICMA), Harbin, China, 6–9 August 2023; IEEE: New York, NY, USA, 2023; pp. 681–686.